Check for updates

Cu-doped SnO$_2$ nanoparticles: size and antibacterial activity investigations

F. F. H. Aragón, [ID] *[ab] L. Villegas-Lelovsky, [ID] *[ac] J. I. Castillo-Llanos, [ID] [a] C. M. Soncco, [ID] [a] J. L. Solis, [ID] [d] G. H. Peralta-Alarcón, [ID] [a] D. G. Pacheco-Salazar [ID] *[a] and P. C. Morais [ID] [be]

Nowadays, the use of self-cleaning surfaces is increasing globally, especially after the COVID-2019 pandemic, and the use of nanoparticles has been shown as a plausible option for this purpose. In the present study, Cu-doped SnO$_2$ nanocrystals were successfully synthesized (in the copper content range of 0–30 mol%) using the polymeric precursor method. The structural, morphological, vibrational, and antibacterial activity were carefully studied to unveil the effect of copper ions on the properties of the hosting matrix, aiming at maximizing the usage of Cu-doped SnO$_2$ nanocrystals. The results show fabrication of nanoparticles near their respective exciton Bohr diameter (5.4 nm for SnO$_2$), however, monophasic SnO$_2$ was observed up to 15 mol%. Above this limit, a secondary CuO phase was observed, as shown by the assessed X-ray diffraction (XRD), Fourier transform infrared, and Raman spectroscopy data. Furthermore, the redshift of the primary A$_{1g}$ vibrational mode of SnO$_2$ is successfully described using the phonon-confinement model, demonstrating a good relationship between the Raman correlation length (L) and the crystallite size ($\langle D \rangle$), the latter determined from XRD. Regarding the antibacterial activity, assessed *via* the disc-diffusion testing method (DDTM) while challenging two bacterial species (*S. aureus* and *E. coli*), our results suggest a rapid diffusion of the nanoparticles out of the paper disc, with a synergistic effect credited to the Sn$_{1-x}$Cu$_x$O$_2$–CuO phases contributing to the inhibition of the bacteria growth. Moreover, the DDTM data scales with cell viability, the latter analyzed using the Hill equation, from which both lethal dose 50 (LD50) and benchmark dose (BMD) were extracted.

1 Introduction

Nowadays, inorganic antimicrobial agents such as semiconductor oxide nanostructures (TiO$_2$, ZnO, CuO, and SnO$_2$) are promising for cleaning surfaces because they are non-toxic, have a high surface-to-volume ratio, visible transparence and have higher thermal stability than organic antimicrobials,[1] which makes it feasible to cover objects like tables, doorknobs, and tactile mobiles to produce self-cleaning antimicrobial surfaces. Besides, SnO$_2$ nanocrystals with small physical dimensions, particularly those around the exciton Bohr diameter,[2] exhibit drastically different properties from their bulk counterparts. The bottom-up method based on chemical synthesis routes of nanocrystals is one method to produce small-size nanoparticles; the final properties of the particles being strongly dependent on the synthesis route. Among the methods used to produce SnO$_2$ nanocrystals, one can list the hydrothermal,[3] sol–gel,[4] co-precipitation,[5] and polymeric precursor methods. Furthermore, after reaching a certain size, nanocrystals can be further engineered by doping, as this seems to be independent of the type of dopant used and the synthesis method.[6–8] Although doping is a highly effective method for manipulating magnetic, electrical, and optical properties of oxide semiconductors, it is an extremely complex process, leading to end properties that are strongly influenced by the position of the dopant ion within the crystal lattice, the final oxidized state, and ionic radii.

By doping oxide semiconductors, such as transition metal-doped SnO$_2$ (TM-SnO$_2$) or earth rare-doped SnO$_2$ nanoparticles, one targets a wide range of applications, including the use of self-cleaning surfaces (SCS). In this regard, one can mention the use of doped SnO$_2$ nanoparticles, which recently gained attention due to antibacterial activity. Studies have shown that these nanoparticles can inhibit the growth of various bacterial species, including Gram-positive and Gram-negative bacteria,[9,10] given that doping enhances antibacterial activity; the highest values reported in the literature are also

*a*Universidad Nacional de San Agustín de Arequipa, Arequipa, Peru. E-mail: ffharagon@gmail.com; leonardo.villegas@unesp.br; dpachecos@unsa.edu.pe

*b*Nucleo de Física Aplicada, Instituto de Física, Universidade de Brasília, Brasília, DF 70910-900, Brazil

*c*Physics Department, IGCE, Paulista State University, CEP 13506-900, SP, Rio Claro, Brazil

*d*Universidad Nacional de Ingeniería, Facultad de Ciencias, Lima, Peru

*e*Catholic University of Brasília, Genomic Sciences and Biotechnology, Brasília, DF 70790-160, Brazil

connected to the maximum doping value employed, as well as the total mass of nanoparticles present in the test. These findings have been described in several studies, where doping metals such as Fe, Co, Ni, Cu, and Ce have been used, and the maximum diameter inhibition zone (DIZ) value has been found for the highest doping concentration and mass of nanoparticles.[9,11–13] In this regard, the report of Sathishkumar *et al.* can be highlighted, displaying and increase in antibacterial activity (using a 10 mm disc) as the doping content and concentration of Cu-doped SnO_2NPs (30, 40, 50, and 60 mg mL^{-1}) increase, leading to the highest DIZ values of 18 and 19 mm for the *S. aureus* and *P. aeruginosa* bacteria, respectively, while using a sample of 9 mol% Cu-doped SnO_2 and 60 mg mL^{-1} concentration.[9] However, the exact mechanism by which doping enhances the antibacterial activity of TM-SnO_2 nanoparticles is not fully understood, although it is believed that the presence of transition metal ions can extend carrier recombination by the increase of defect centers, acting as trapping cores. This can lead to an increase in the generation of superoxide ($^\bullet O^{-2}$), $O^2 + e^- \rightarrow {}^\bullet O^{-2}$, which is the precursor of other reactive oxygen species (ROS), being responsible for the antibacterial effect of TM-SnO_2 nanoparticles.[14] ROS have a strong ability to oxidize a wide range of organic-based materials, such as pollutants, bacteria, cancer cells, and viruses. When doped oxide semiconductors are used as self-cleaning surfaces, the ROS generated on the surface can cause oxidative stress in bacterial cells, destroying cell walls, DNA, and relevant proteins.[6] The research of new materials with SCS activity is of extreme importance, especially after the COVID-2019 pandemic. In this scenario, we can highlight the use of Cu-doped oxide semiconductor with high antibacterial activity while it is irradiated with UV light.[15] However, UV light is not feasible for creating self-cleaning and antibacterial surfaces in typical indoor conditions, with negligible UV light exposition. Therefore, it is necessary to search for alternatives aiming at to increase antimicrobial response in a dimly illuminated environment. Also, no previous investigation has been carried out to evaluate the influence of doping enrichment of the surface and the onset of a secondary phase on the antibacterial activity of the system, indicating a knowledge gap.

In this study, we aim to investigate the synthesis and characterization of Cu-doped SnO_2 nanoparticles, with emphasis on structural, morphological, and vibrational properties plus antibacterial activity against *Escherichia coli* (ATCC® 33876) and *Staphylococcus aureus* (ATCC® 25923) in a dark environment. We also explore the possible mechanisms by which Cu-doping contributes to enhance the antibacterial activity of the as-synthesized SnO_2 nanoparticles. Our findings are expected to contribute to the development of novel materials for self-cleaning surfaces with high antibacterial activity.

2 Experimental details

Cu-doped SnO_2 nanocrystals were synthesized using the polymeric precursor method (Pechine's method), using tin chloride monohydrate ($SnCl_2 \cdot H_2O$), copper nitrate hexahydrate ($Cu(NO_3)_3 \cdot 6H_2O$), ethylene glycol ($C_2H_4(OH)_2$) and citric acid ($C_6H_8O_7$)as reactive chemicals. More details about the used synthesis protocol have been described in the literature.[16] X-ray diffraction (XRD) measurements were performed using a Rigaku MiniFlex 600 X-ray diffractometer equipped with Cu Kα radiation ($\lambda = 1.5418$ Å) and scanning in the 2θ range of 20–80°. Scanning electron microscope (SEM) images were obtained using a Zeiss microscope, model EVO10, and JEOL Scanning Electron Microscopy (SEM) model JSM 7001F, where X-ray energy dispersive spectroscopy (EDS) is implemented to determine the chemical composition of the samples. Transmission electron microscopy (TEM) images were obtained using a Talos™ F200i commercial microscope. Fourier-transform infrared spectroscopy (FTIR) measurements were carried out (samples pressed in KBr pellet) using a Bruker VERTEX 70 FT-IR spectrometer, scanning in the wavenumber range of 450–4000 cm^{-1}. Room temperature Raman spectra were recorded using a Horiba Labram HR Evolution spectrometer equipped with the 532 nm laser line. The agar disc-diffusion testing method (DDTM) was used to evaluate the inhibition zone (IZ) associated with the *S. aureus* and *E. coli* species. The DDTM is made up of a fixed amount (5 mg) of Cu-doped SnO_2 nanocrystal impregnated on filter paper discs (6 mm of diameter), which are placed on the surface of a Petri dish culture medium (Mueller–Hinton agar) containing the appropriate bacterium (*S. aureus* or *E. coli*). After placing the paper discs, the Petri dish was placed in an incubation chamber kept at 35 °C for 24 and 48 hours for *E. coli* and *S. aureus*, respectively, with the *in vitro* tests performed in triplicate (×3).

3 Results and discussions

XRD patterns of undoped and Cu-doped SnO_2 nanoparticles are shown in Fig. 1(a). The main crystalline phase is linked with the rutile tetragonal unit cell SnO_2 phase, as indicated by the main peaks found at 26.5°, 33.8°, 37.9° and 51.7° associated with the (110), (101), (200) and (211) plane reflections, respectively. However, additional peaks at 35.5° and 38.7° were observed in copper concentrations starting from 20%, which have been respectively linked with the (111) and (022) planes of the secondary CuO phase; the latter suggesting that the solution limit is lower than 20 mol%, this being due to the detection limit of the technique.

To determine the structural parameters the XRD patterns were analyzed using Rietveld refinement implemented in EXPGUI, a graphical user interface for GSAS software,[8] where a Lorentzian peak shape (S) was used to model the diffraction peaks profiles, $S = X/\cos\theta + Y\tan\theta$, with the first term representing the Lorentzian Scherrer whereas the second term describes the strain broadening. A typical fit is shown in Fig. 1(b), where the open black circles are the recorded experimental data, the solid red line is the theoretical curve, and the solid green line at the bottom is the difference between them.

Table 1 displays the structural parameters extracted from the Rietveld refinement. The lattice constants for the undoped SnO_2 nanoparticles are $a = b = 4.7339$ Å and $c = 3.1894$ Å, giving a unit cell volume of 71.374 Å^3. However, the unit cell volume shows an increasing tendency as the Cu-content increases,
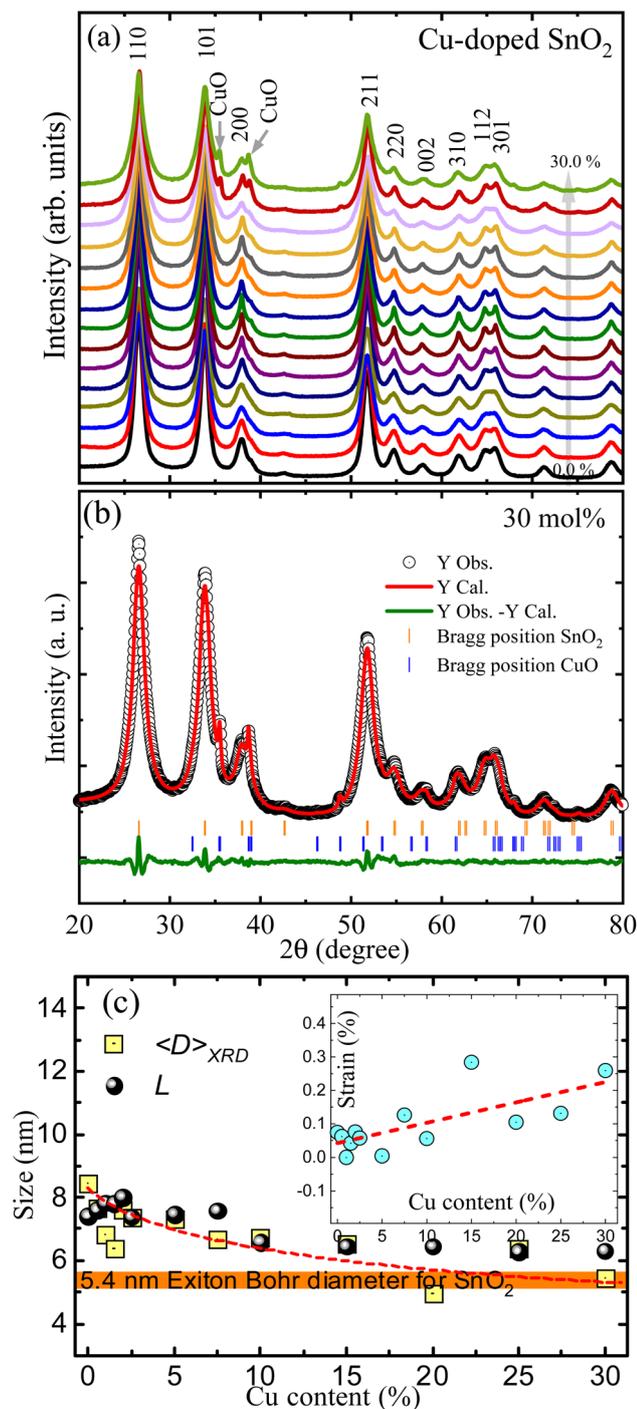
Fig. 1 (a) XRD patterns of the undoped and Cu-doped SnO_2 nanoparticles. (b) Rietveld refinement of the 30 mol% Cu-doped SnO_2. The open black circles are the record data, the solid red line is the calculated, and the solid green line is the difference between them. (c) Crystallite size as a function of the nominal Cu-content, where the Raman correlation length (L) was included. The inset shows the residual strain.

which is related to the entry of Cu^{2+}-ions with ionic radii of 0.73 Å in solid solution with Sn^{4+}-ions with ionic radii of 0.69 Å, both in six-coordinate geometry.[17] It is worth noting that if the Cu^{2+}-

ions entered the SnO_2 crystal lattice with a low spin state (ionic radii of 0.54 Å) this could cause an opposite trend, as shown by Sathishkumar *et al.* while observing a decrease in the lattice parameters.[9] Using the quasispherical particle's Scherrer constant (0.9), the mean crystallite size ($\langle D \rangle_{XRD}$) of the Cu-doped SnO_2 nanoparticles was calculated from Scherrer's broadening contribution. The results are shown in Fig. 1(c), where one can see the decreasing trend (from $\sim$9 nm to $\sim$5 nm) as the Cu content increases. Fig. 1(c) emphasizes (horizontal orange color strip) the SnO_2 exciton Bohr diameter, which is around 5.4 nm,[2] meaning that a quantum confinement effect cannot be ruled out for the samples, as it will be explained below.

SEM and EDS measurements were performed in some of the samples to determine their chemical composition. Fig. 2 shows the SEM image and its corresponding EDS map for the undoped (upper panel) and 30 mol% Cu-doped SnO_2 (lower panel). The SnO_2 nanocrystals exhibit a curious morphological characteristic, akin to dried sludge-like formations, which is a result of the high-temperature production method. Meanwhile, or the 30 mol% Cu-doped a more porous structure is observed, which could be correlated with the CuO structure. To make an elemental characterization, a small and homogeneous structure was chosen from both samples (see dashed lines in Fig. 2) and the EDS analysis was performed on it. For the undoped SnO_2, the EDS spectrum (see right-hand side of Fig. 2) displays the characteristic X-ray peaks located at 0.52 keV and 3.4 keV, expected for the O Kα and Sn Lα, respectively. No additional characteristic X-ray peaks are observed, confirming the single SnO_2 crystalline phase observed by XRD. However, for the Cu-doped samples, two additional X-ray peaks are seen located at 0.93 and 8.04 keV; respectively associated with the characteristic Cu Lα and Cu Kα x-rays. The calculated Cu/(Cu + Sn) weight ratio collected in Table 1, was obtained by deconvolution of the characteristic X-ray peaks, performed in the internal EDS software. The results are consistent with the nominal increase of Cu-content used in the Cu-doped nanocrystals synthesis.

In addition, TEM images were recorded and corroborated with the crystallite size obtained from the XRD analyses. Fig. 3(a) shows a representative high-resolution TEM (HRTEM) image obtained for the 2.5 mol% Cu-doped SnO_2 nanocrystals, where the interplanar spacing (0.33 ± 0.01 nm) corresponds to the main crystal plane (110) of the SnO_2 phase. Fig. 3(b) depicts a representative TEM image of the recorded micrographs used to analyze the samples' morphology, revealing quasispherical particles from which the physical particle size distribution was obtained. Particles' counts were made using the ImageJ software,[18] to assess their diameter,[18] where $N = 405$ particles were counted and used for building the particle size histogram while following the Sturges method[19] (see Fig. 3(c)). The histogram's binwidth (W) is obtained from the relationship: $W = (D_{Max} - D_{Min})/k$, where $k = 1 + 3.322 \log(N)$. The histogram was modeled by a lognormal distribution function, $f(D) = (1/\sigma D\sqrt{2\pi})\exp(-\ln^2(D/D_0)/2\sigma^2)$, where D_0 is the median and σ is the polydispersity index of the distribution. After analyses, an average particle size $\langle D \rangle = D_0 \exp(\sigma^2/2) =$

Table 1 Lattice parameters obtained from the Rietveld refinement. Also, the chemical composition Cu/(Cu + Sn) was included for some nanopowders with standard deviation values around 20 mol%

Cu (mol%)	SnO$_2$ phase			CuO phase				Cu/(Cu + Sn)
	a (Å)	c (Å)	V (Å^3)	V (Å^3)	$\langle D \rangle_{XRD}$ (nm)	%		mol%/mol%
0.0	4.7339	3.1849	71.374	—	—	—		—
0.5	4.7344	3.1849	71.389	—	—	—		0.7
1.0	4.7329	3.1840	71.323	—	—	—		1.2
1.5	4.7349	3.1857	71.421	—	—	—		—
2.0	4.7344	3.1848	71.385	—	—	—		—
2.5	4.7332	3.1842	71.338	—	—	—		—
5.0	4.7345	3.1845	71.381	—	—	—		—
7.5	4.7339	3.1838	71.346	—	—	—		—
10.0	4.7340	3.1839	71.353	—	—	—		—
15.0	4.7357	3.1858	71.447	—	—	—		15.4
20.0	4.7338	3.1848	71.369	81.045	96	1		23.2
25.0	4.7344	3.1844	71.377	81.047	39	5		25.7
30.0	4.7356	3.1857	71.444	81.198	32	6		38.4

8.6 nm was obtained, in very good agreement with the values extracted from the XRD examinations (see Fig. 1(c)).

Fig. 4 depicts the FTIR spectrum of the Cu-doped SnO$_2$ nanocrystals at wavenumber (ω) ranging from 4000 to 400 cm^{-1}. Visual inspection reveals bands present in the undoped SnO$_2$ nanocrystals, which be divided into three ranges. First, for wavenumber between 4000 and 2500 cm^{-1}, the OH band is observed at ~3426 cm^{-1},[20,21] the CH$_2$ asymmetric stretching (AS) band is observed at ~2924 cm^{-1}, and the CH$_2$ symmetric stretching (SS) band is observed at ~2853 cm^{-1}. Second, from intermediate wavenumber, ranging from 2000 to 1500 cm^{-1}, the bending mode of surface water molecules and OH groups is observed at ~1634 cm^{-1}, as described in the literature.[22] Third, in the wavenumber range from 700 to 400 cm^{-1}, the skeletal Sn–O vibrations of the SnO$_2$ structure are shown, which are located around 652 cm^{-1}.[23] Moreover, with the introduction of copper, several changes can be observed, such as a shift of the Sn/Cu–O skeletal vibrations induced by copper addition on the host lattice, and the increase of the absorbed bands (see Fig. 4(a)), indicating an
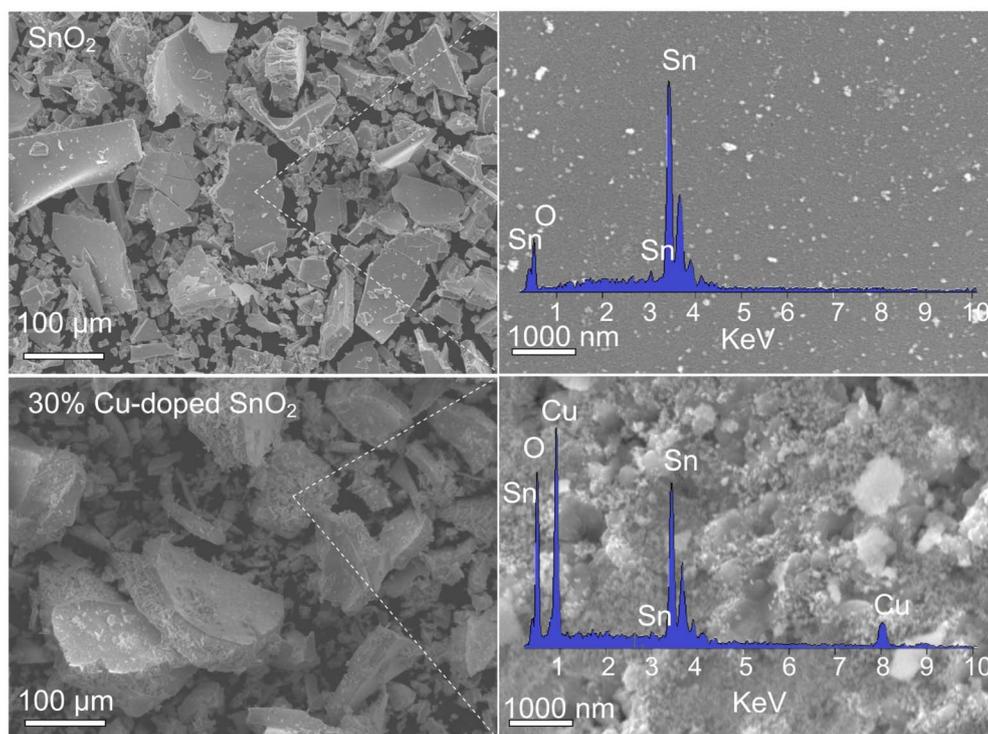
Fig. 2 SEM (left panels) and EDS (right panels) images of the undoped (upper panels) and 30 mol% (lower panels) Cu-doped SnO$_2$ were used to determine the chemical ratio Cu/(Cu + Sn).
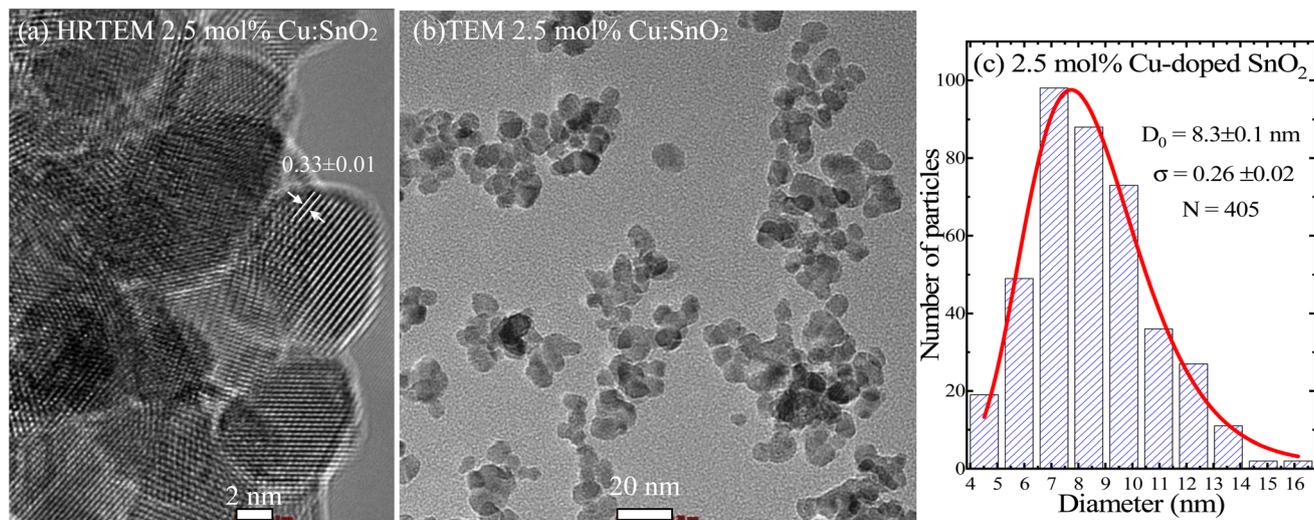
Fig. 3 (a) HRTEM of the 2.5 mol% Cu-doped SnO_2 nanocrystal showing a representative interplanar distance (0.33 ± 0.01 nm). (b) Representative TEM image of the 2.5 mol% Cu-doped SnO_2 sample. (c) Corresponding particle size histogram.

enhancement of the absorbed region on the nanoparticle surface as the Cu-content increases. In view of the aforementioned points, the spectra were curve-fitted assuming Gaussian-shaped peaks. Fig. 4(b) shows the peak wavenumber position *versus* Cu-content for the skeletal Sn–O vibrational region fitted with two peaks (ω_1 and ω_2); these two peaks are the minimum number of peaks to achieve a reasonably good fit about the Sn/Cu–O vibration zone. The inset in Fig. 4(b), shows the spectrum fitting of the 30.0 mol% Cu-doped SnO_2 sample, where the peaks around 510–530 cm^{-1} and 650–670 cm^{-1} are herein referred to as ω_1 and ω_2, respectively. Hooke's law was used to model the frequency dependence on the Cu-content, with $\omega \propto \sqrt{k/\mu}$, where k and μ are the force constant and the reduced mass, respectively. Considering μ between Sn–O (14.1 g mol^{-1}) and Cu–O (12.8 g mol^{-1}), an increase in ω for a monotonic substitution of Sn for Cu-ions is expected, thus explaining the increase from 1.5 to 10 mol% (zone II, in Fig. 4(b)) for the two frequencies (ω_1 and ω_2). However, it does not explain the decreasing tendency of ω in the first doping zone, up to 1.5 mol% (zone I), and for high concentrations, *i.e.* above 10 mol% (zone III). Regarding the low doping zone (zone I), a plausible explanation could be associated with the first annihilation of intrinsic defects such as oxygen vacancies (V_O) present in the undoped sample. Meanwhile, in the high copper concentration (zone III), the observed trend could be correlated with the segregation of Cu-ions and the nucleation process of the onset CuO phase. Considering the intensity rise in the absorption bands (see Fig. 4(c)), one can extract the ratio between the areas (integrated intensity) of the absorbed O–H bands (~3426 and ~1634 cm^{-1}) and the skeletal Sn–O bands. In this regard, the integrated intensity ratio (I_{O-H}/I_{Sn-O}) between the adsorbed molecules (such as O–H) and skeleton (Sn–O) vibrational bond (I_{O-H}/I_{Sn-O}) can be related through the crystalline particle size determined from the XRD data, in agreement with the following equation.[24]

$$\left(\frac{I_{O-H}}{I_{Sn/Cu-O}}\right)^3 \propto \left(\frac{\text{surface area}}{\text{volume}}\right)^3 \propto \frac{1}{\langle D \rangle_{XRD}^3} \quad (1)$$

where $\langle D \rangle_{XRD}$ is the crystallite size obtained from the XRD analyses. Using eqn (1), the solid red line in Fig. 4(c) represents the best fit of the experimental data. The latter is a crucial finding once it predicts that the surface's reactivity will rise due to the ability to absorb, regulated by the Cu-content, which is consistent with the decrease in crystallite size indicated by XRD examination.

Fig. 5(a) shows the room-temperature Raman spectra of undoped and Cu-doped SnO_2 nanocrystals. At first glance, one can observe the presence of many bands, that can be grouped into structural and disordered modes (S_1, S_2, and S_3). Regarding the structural modes, one can begin with the modes located at low frequencies, between 200 and 400 cm^{-1}, which are labeled $E_u^{(1)}$, $E_u^{(2)}$(LO) and $E_u^{(2)}$(TO), followed by modes located at frequencies between 400 and 800 cm^{-1}, namely E_g, A_{1g} and B_{2g}, which are respectively located at 471.7, 628.9, and 769.7 cm^{-1} in the undoped SnO_2 nanopowder. The A_{2u}(LO) mode is also observed at ~686 cm^{-1}, although it is hidden by the S_3 mode, especially at higher Cu-doping. These modes have been extensively studied and reported in the literature.[25–27] At this stage, it is crucial to elucidate how Cu-ions alter the vibrations in the SnO_2 host matrix. In this regard, Fig. 5(a) shows the spectrum (upper panel) of the 30 mol% Cu-doped SnO_2 nanocrystal, with two vibrational modes located at ~276 and ~333 cm^{-1}, which are missing in the undoped SnO_2 sample. These modes were found to be consistent with the main A_g and B_{2g} modes of monoclinic CuO respectively at ~275 and ~329 cm^{-1}, reported by Shen *et al.*[28] Formation of a secondary CuO phase, observed by Raman spectroscopy, is consistent with the secondary crystalline phase found in the XRD measurements. Furthermore, the A_g and B_{2g} modes associated with the CuO phase drop down when the Cu-doping lowers, which is associated with the reduction of the secondary phase. On the other hand, the
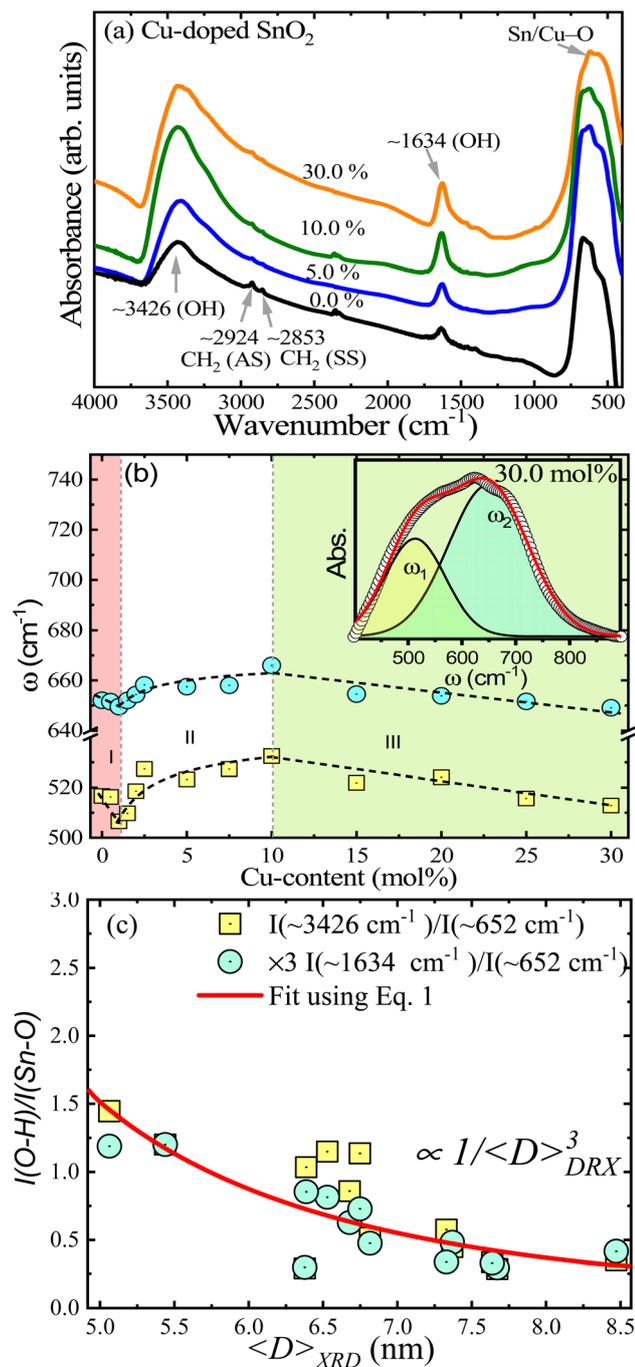
Fig. 4 (a) FTIR of the undoped and Cu-doped SnO$_2$ nanocrystals. (b) Wavenumber *versus* Cu-content for the skeletal Sn–O vibrational ranges. (c) Integrated intensity ratio between the adsorbed molecules, such as O−H and skeleton Sn/Cu−O vibration bond length.

Fig. 5 (a). Room temperature Raman spectra of undoped and Cu-doped SnO$_2$ nanocrystals. (b) Raman shift of the A$_{1g}$ vibrational mode as a function of the inverse of the nanoparticle's radius (1/R) for the Cu-doped SnO$_2$.

disordered S$_1$ and S$_2$ modes (located at ∼500 and ∼560 cm^{-1}), with respect to the canonical A$_{1g}$ mode, show a decreasing tendency with the increasing Cu content. This finding means that the disorder on the particle surface is reducing, possibly due to the elimination of surface defects, such as oxygen vacancies, caused by gradual enrichment of the surface with Cu-ions, leading the surface energy to decline while increasing the
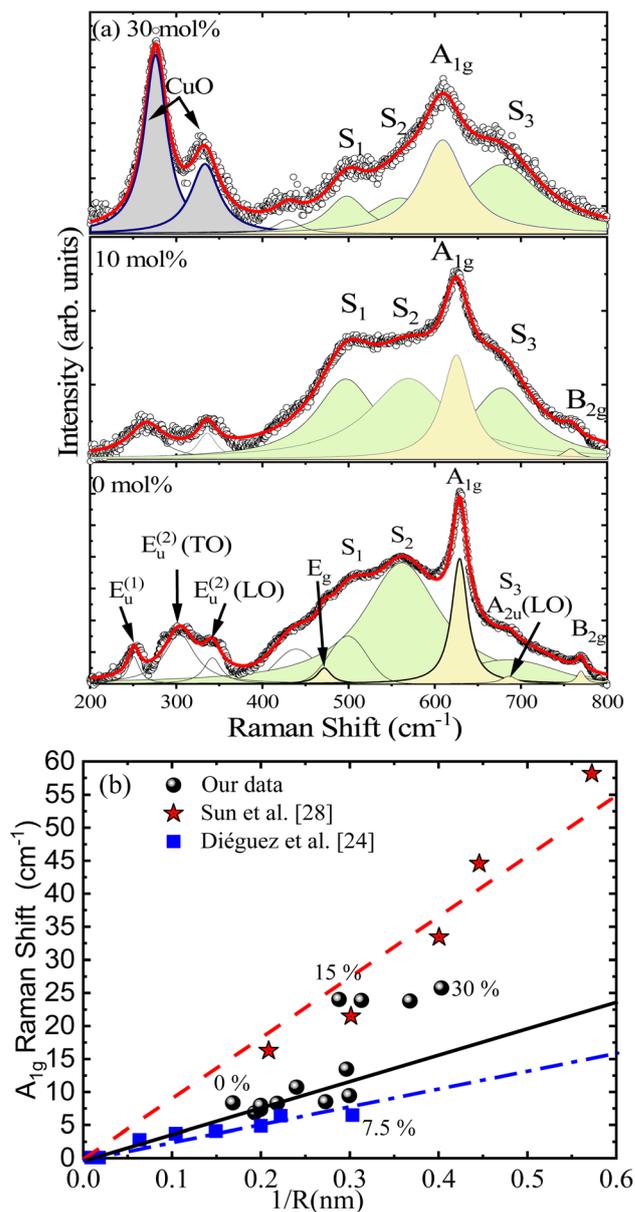
surface area, in agreement with the Ostwald ripening model.[29] Similar behavior is displayed in Sn$_{1-x}$Co$_x$O$_2$ nanoparticles.[7] The effect of the Cu-doping is analyzed in more detail while investigating the dominant A$_{1g}$ mode, which exhibits a redshift and FWHM increase associated with the increase in the surface disorder degree provoked by continuous reduction in crystallite size. With the above consideration in mind, Fig. 5(b) depicts the Raman shift as a function of the inverse of the nanoparticle's radius (1/R) for the Cu-doped SnO$_2$, with a linear increasing trend up to 7.5 mol% Cu-content. It is worth mentioning that the same tendency is reported for Sun *et al.*[30] and Diéguez *et al.*[26] for undoped SnO$_2$, as included in Fig. 5(b) for comparison.

However, our data display a breaking of the linearity in the range of 7.5–15 mol%, keeping the crystallite size of the SnO$_2$ phase almost unchanged in this range. This fact could be correlated with the enrichment of the surface exactly when the nucleation process is beginning, suggesting a strong redshift in this region. It is worth noting that above this range (7.5–15 mol%), the Raman shift is unaffected because excess of Cu-ions are converted into the CuO secondary phase.

Furthermore, regarding the prominent A$_{1g}$ Raman mode, the shift to lower frequency accompanied by a broadening are signatures of the phonon confinement effect, as suggested in the literature.[31] In this scenario, the phonon confinement is induced by the crystallites' low dimension, introducing a reduction of the correlation length of the phonons as the wave vector selection rule is relaxed. In this scenario, within the phonon-confinement model (PCM), the A$_{1g}$ Raman line intensity can be described by:

$$I(\omega) = \int \frac{d^3 q |C(0,q)|^2}{[\omega - \omega_S - \omega(q)]^2 + (\Gamma_0/2)^2} \quad (2)$$

where $|C(0,q)|^2$ is the weighting function, Γ_0 is the natural linewidth, ω is the phonon frequency and ω_S is a parameter correlated with the strain-induced phonon shift.[32] In order to describe the phonon confinement, the Gaussian weighting function has been used as a first approximation in the phonon dispersion relation. However, a higher correlation was found while using $\sin(\alpha r)/\alpha r$ modulating at the weighting function (see eqn (3)), as proposed in the literature,[33] where L is the correlation length, taken as the nanocrystallite's diameter.

$$|C(0,q)|^2 \cong \frac{\sin^2(qL/2)}{(4\pi^2 - q^2 L^2)^2} \quad (3)$$

Fig. 6(a) shows the fit of the A$_{1g}$ Raman mode using eqn (2) and (3) for undoped and 30 mol% Cu-doped SnO$_2$, revealing an excellent correlation with the experimental data. Fig. 1(c) presents the Cu-content dependence of the Raman correlation length (L) and the crystallite size ($\langle D \rangle_{XRD}$) obtained from the XRD data, indicating a good correlation between them. It is also worth noting that the strain-induced shift term (ω_S) was critical to achieve a satisfactory fit. The Cu-content dependence of the strain-induced shift term (ω_S) is shown in Fig. 6(b). Additionally, in order to elucidate the underlying detailed mechanisms, one should mention that compressive strain induces a linear blue-shift in the A$_{1g}$ vibrational mode, as reported by Girao *et al.*[34] Moreover, it is important to note that this behavior is consistent with the shift in the skeletal Sn–O bonds detected by FTIR analysis, which specifically shows a singularity in this region. Taking this into consideration, the enrichment region detected in this zone induces strong strain, primarily on the nano-particle's surface.

4 Antibacterial application

To demonstrate the potential application of Cu-doped SnO$_2$ nanocrystals as an antibacterial material, two types of bacterial cultures were studied: Gram positive bacteria, *Staphylococcus aureus* (*S. aureus*) and Gram negative bacteria, *Escherichia coli*
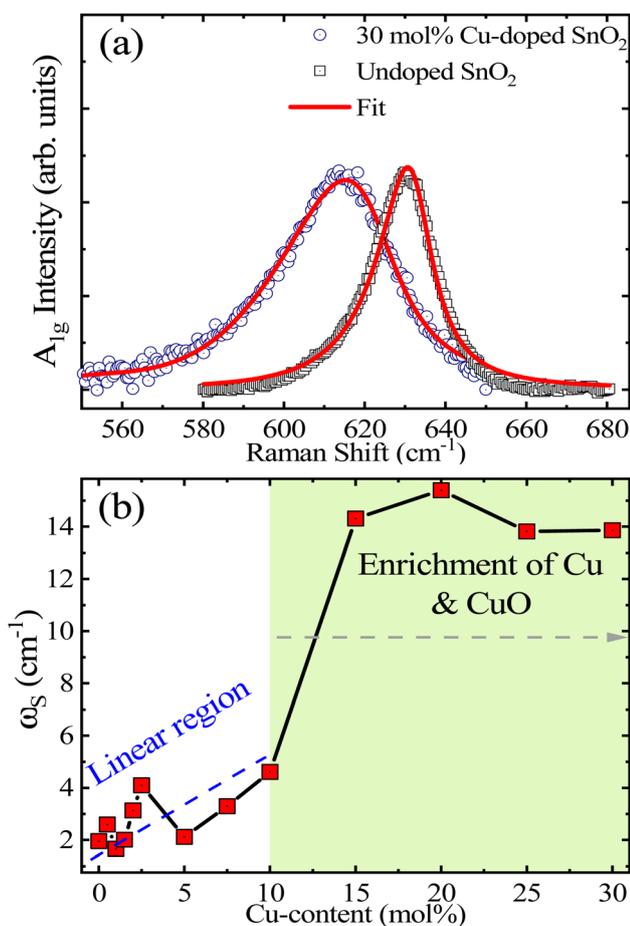

Fig. 6 (a) Fit of the A$_{1g}$ Raman mode using the PCM for undoped and 30 mol% Cu-doped SnO$_2$. (b) Strain-induced shift term *versus* Cu-content.
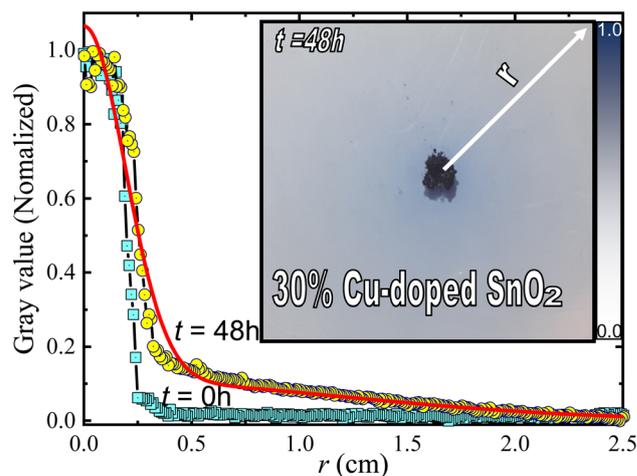

Fig. 7 Profile of the change of the gray color as a function of the distance (*r*) for time (*t*) 0 and 48 hours. The inset displays the change in color after 48 hours.

(*E. coli*). The *in vitro* disc diffusion method was used to assess the antibacterial activity of both species. Once nanoparticles are added to the culture media (agar), they begin to diffuse radially and expand until they reach a specific area. As the radial distance (r) increases, the concentration of the particles changes. The latter can be visualized by performing a simple experiment with only nanoparticles widespread on the agar medium (without any type of bacteria), as shown *via* the color change around the center of the sample's spot over a period of 48 hours for the 30 mol% Cu-doped SnO$_2$ nanoparticles (see Fig. 7). The extent of the color change can be measured using a gray value profile. Fig. 7 clearly demonstrates the difference in the profile obtained at $t = 0$ h and $t = 48$ h. To model this change, one can use an approach where the color intensity is proportional to the nanoparticle's concentration (φ). The second Fick's law, which describes the diffusion over time, can be applied to model the two dimensional nanoparticle's diffusion:

$$\frac{\partial \varphi}{\partial t} = \text{Dif} \frac{\partial^2 \varphi}{\partial r^2} \qquad (4)$$

where φ is the nanoparticle's concentration for a specific time (t) and distance (r) and Dif is the diffusion coefficient. Solution of eqn (4) can be expressed as a linear combination of two thin film tracer solutions, where λ_1 and λ_2 are normalization constants:

$$\varphi(r, t) = \frac{\lambda_1}{\sqrt{4\pi \text{Dif}_1 t}} \exp\left(-\frac{r^2}{4\text{Dif}_1 t}\right)$$
$$+ \frac{\lambda_2}{\sqrt{4\pi \text{Dif}_2 t}} \exp\left(-\frac{r^2}{4\text{Dif}_2 t}\right) \qquad (5)$$

The solid red line in Fig. 7 represents the best fit of the data (yellow circles) using eqn (5). The values obtained for the diffusion coefficients are $\text{Dif}_1 = 10.5(1) \times 10^{-6}$ cm^2 s^{-1} and $\text{Dif}_2 = 4.0(6) \times 10^{-6}$ cm^2 s^{-1}, representing the nanoparticle's diffusion nearest and farthest center of the sample's spot, respectively. The latter diffusion coefficient is of the order of those reported for metronidazole, chloramphenicol succinate, cefsulodin and piperacillin antibiotics, with diffusion coefficients ranging from 0.6×10^{-6} to 1.2×10^{-6} cm^2 s^{-1} in agar.[35] Fig. 8 shows the final inhibition zone (IZ) for *E. coli* and *S. aureus* after 24 and 48 hours, respectively. As can be seen, there is a strong relationship between IZ and Cu-content, for both bacteria species. The latter is in agreement with the report of Sathishkumar *et al.*, who report an increase in the antibacterial activity as the copper content.[9] A possible explanation for this finding is based on the values of the diffusion coefficients (Dif) of the nanoparticles, presenting an inverse dependence on the particle size ($\langle D \rangle$), as described by the Stokes–Einstein equation $\text{Dif} = kT/3\pi\eta\langle D \rangle$, where k is the Boltzmann constant, T is the absolute temperature, and η is the dynamic viscosity. However, in a more recent report, Peulen and Wilkinson suggested that the diffusion coefficient (Dif) decreases exponentially with the square of nanoparticle size.[36] In both cases, this implies that small particles reach a larger area, which explains well the
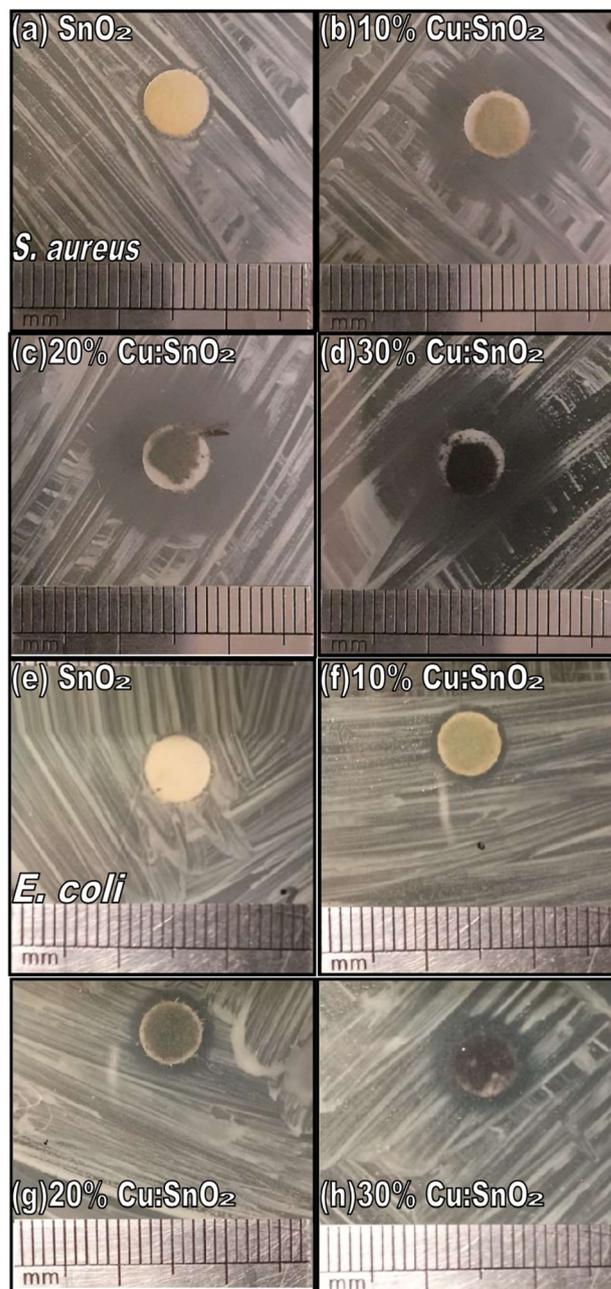

Fig. 8 Undoped and Cu-doped SnO$_2$ nanoparticles' antibacterial activity under dark conditions. (a) SnO$_2$, (b) 10 mol%, (c) 20 mol%, and (d) 30 mol% Cu-content for *S. aureus* and (e) SnO$_2$, (f) 10 mol%, (g) 20 mol%, and (h) 30 mol% Cu-content for *E. coli*.

systematic increase of the inhibition zone. Surprisingly, however, the system shows a discontinuity in the bacterial growth (around 7.5–10 mol% Cu), with a significantly higher antibacterial activity for higher Cu-doping (above 7.5–10 mol% Cu), even more active than pure CuO nanoparticles with a crystallite size of ~23 nm. This information is emphasized in Fig. 9(a), with the help of the horizontal solid green line, where CuO nanoparticles were tested under the same conditions as the Cu-doped SnO$_2$ nanocrystals. Our findings strongly suggests that a mechanism of inhibition of bacteria growth can be
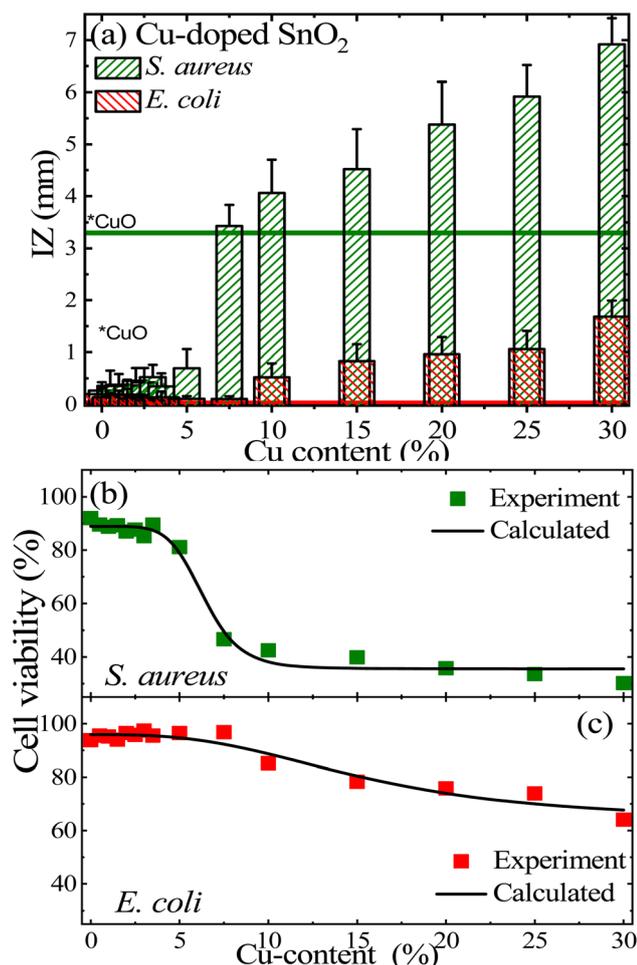
Fig. 9 (a) Inhibition zone (IZ) thickness obtained from the *in vitro* disc diffusion method, using undoped and Cu-doped SnO₂ nanoparticles. (b) and (c) Cell viability (C_V) *versus* Cu-content for the *S. aureus* and *E. coli*, respectively, with symbols representing experimental data and solid black lines representing the best fittings using eqn (6).

correlated with copper enrichment of the SnO₂ nanoparticles' surface and the onset of a synergistic effect with the secondary CuO phase, the latter potentially producing high ROS content, which would be responsible for the observed strong antibacterial activity.

Importantly, Fig. 9(a) shows the results of the aforementioned IZ data, characterized by its diameter thickness (d_{IZ}), herein measured in units of millimeters (mm). Moreover, in the *in vitro* disc diffusion method, the reference diameter (d_R) is taken as the diameter of the disc paper impregnated with the testing sample. Regarding the type of bacteria under test, our study evidenced that the Cu-doped SnO₂ nanocrystals are more efficient for Gram-positive *S. aureus* than for Gram-negative *E. coli*. This effect was also reported by Alotaibi *et al.* who used thin films of Cu-doped anatase (TiO₂) on glass substrates to test the bactericidal activity of these two bacterial species.[15] Therefore, it is quite obvious that the IZ data scales with the cell viability (C_V). In this regard, one can claim that C_V scales linearly (first approximation) with d_R/d_{IZ}, namely $C_V = (d_R/d_{IZ}) \times 100(\%)$. This

is indeed a pioneering proposal. Fig. 9(b) and (c) shows the cell viability *versus* Cu-content in the doped SnO₂ nanoparticles for *S. aureus* and *E. coli*, respectively. The cell viability data (solid square symbols) are curve-fitted (solid black lines) using the Hill equation, successfully applied to assess the viability data of nanomaterials, as recently reported by Li *et al.*:[37]

$$C_V = V_0 - V_1 \frac{C^n}{K + C^n} \qquad (6)$$

where V_0 and V_1 are normalization parameters, C is the Cu-content (mol%), n is the Hill coefficient, and K describes the binding constant between the nanoparticle and the bacteria membrane. The Hill coefficient (n) represents the cooperativity index and describes two different biological scenarios for binding of the Cu-doped SnO₂ nanoparticles onto the cell surface: (a) $n > 1$ signaling positive cooperativity, *i.e.* the binding of the first nanoparticle increases the affinity for binding others or (b) $n < 1$ signaling negative cooperativity, *i.e.* the binding of the first nanoparticle reduces the affinity for binding others. The fitting parameters (V_0, V_1, n, and K) were (88.9, 53.0, 6.7, and 2.3×10^5) and (95.9, 32.0, 2.9, and 2.7×10^3) for *S. aureus* and *E. coli*, respectively. Moreover, from the four fitting parameters one can extract the lethal dose 50 (LD50) and the benchmark dose (BMD), herein representing the Cu-doping level required to reduce the bacteria population by 50% and 10%, respectively. Calculation can be performed using the following equations:

$$LD50 = \left[\frac{K}{2(V_1/V_0) - 1}\right]^{1/n} \qquad (7)$$

and

$$BMD = \left[\frac{K}{10(V_1/V_0) - 1}\right]^{1/n} \qquad (8)$$

where the values found for the doses (LD50 and BMD) were (8.1 mol% and 5.0 mol%) for *S. aureus* and (22.9 mol% and 11.5 mol%) for *E. coli*.

Impressively, as far as the cytotoxicity is concerned, the cell viability evaluation herein employed with the help of the Hill equation, signaling LD50 above 7.5 mol% Cu for both bacterial species, corroborates with the outcomes of the IZ *in vitro* disc diffusion method, the latter revealing higher antibacterial activity for Cu-doping above 7.5–10 mol% Cu. Likewise, the numbers assessed for LD50 and BMD are in excellent agreement with the higher antibacterial activity towards *S. aureus*. Furthermore, the Hill coefficient (n) associated with *S. aureus* (6.7) is higher than the value associated with *E. coli* (2.9), signaling higher antibacterial activity to the former.

5 Conclusions

In this study, we report on the plausible use of Cu-doped SnO₂ nanoparticles to create self-cleaning surfaces. In this regard, we have systematically studied the influence of the Cu-dopant within SnO₂ nanoparticles (NPs). The synthesis process involved the preparation of a polymer solution containing precursors of both copper and tin ions (precursor polymeric method), with the copper concentration varying from 0 to

30 mol%. X-ray diffraction (XRD) was performed to analyze the crystal structure of the synthesized nanoparticles. It was found that the lattice constants increased with increasing Cu content, which is in good agreement with the difference in ionic radii between Cu and Sn-ions. Fourier transform infrared measurements showed vibrational modes (O–H, C–H, and C–O) at the expected positions. However, a shift to higher values was observed for the skeletal Sn–O band. This suggests a change in the reduced mass associated with the entry of Cu-ions. Raman measurements were performed on all samples to investigate any changes in their vibration properties as the amount of Cu content was increased. Furthermore, a significant antibacterial effect over the CuO has been detected through a bioassay. The disc-diffusion testing method (DDTM), performed with two bacterial species (*S. aureus* and *E. coli*), was used to assess the inhibition of bacteria growth. It was found that the DDTM data scales with cell viability, the latter analyzed using the Hill equation, from which both lethal dose 50 (LD50) and benchmark dose (BMD) were extracted. The ulterior functionalization of this type of metal oxide powder can be used for self-cleaning surfaces protocols.

Conflicts of interest

The authors declare no conflict of interest.

Acknowledgements

References

1 G. E. Yılmaz, I. Göktürk, M. Ovezova, F. Yılmaz, S. Kılıç and A. Denizli, *Hygiene*, 2023, **3**, 269–290.

2 X. Xu, J. Zhuang and X. Wang, *J. Am. Chem. Soc.*, 2008, **130**, 12527–12535.

3 W. Hu and X. Yuan, *J. Nanomater.*, 2017, **2017**, 6976203.

4 G. H. Patel, S. H. Chaki, R. M. Kannaujiya, Z. R. Parekh, A. B. Hirpara, A. J. Khimani and M. P. Deshpande, *Phys. B*, 2021, **613**, 412987.

5 S. Naz, I. Javid, S. Konwar, K. Surana, P. K. Singh, M. Sahni and B. Bhattacharya, *SN Appl. Sci.*, 2020, **2**, 975.

6 P. Sivakumar, H. S. Akkera, T. R. Kumar Reddy, Y. Bitla, V. Ganesh, P. M. Kumar, G. S. Reddy and M. Poloju, *Opt. Mater.*, 2021, **113**, 110845.

7 F. F. H. Aragón, L. Villegas-Lelovsky, L. Cabral, M. P. Lima, J. C. R. Aquino, M. C. Mathpal, J. A. H. Coaquira, S. W. da Silva, L. C. C. M. Nagamine, S. O. Parreiras, P. L. Gastelois, G. E. Marques and W. A. A. Macedo, *Phys. Chem. Chem. Phys.*, 2020, **22**, 3702–3714.

8 B. Toby, *J. Appl. Crystallogr.*, 2001, **34**, 210–213.

9 M. Sathishkumar and S. Geethalakshmi, *Mater. Today: Proc.*, 2020, **20**, 54–63.

10 Bhawna, A. K. Choudhary, A. Gupta, S. Kumar, P. Kumar, R. P. Singh, P. Singh and V. Kumar, *Front. Nanotechnol.*, 2020, **2**, 2673–3013.

11 D. Toloman, A. Popa, M. Stefan, T. D. Silipas, R. C. Suciu, L. Barbu-Tudoran and O. Pana, *Opt. Mater.*, 2020, **110**, 110472.

12 A. Podurets, M. Khalidova, L. Chistyakova, N. Bobrysheva, M. Osmolowsky, M. Voznesenskiy and O. Osmolovskaya, *J. Alloys Compd.*, 2022, **926**, 166950.

13 A. B. Ali Baig, V. Rathinam and V. Ramya, *Mater. Technol.*, 2021, **36**, 623–635.

14 R. Pandiyan, S. Mahalingam and Y.-H. Ahn, *J. Photochem. Photobiol., B*, 2019, **191**, 18–25.

15 A. M. Alotaibi, B. A. D. Williamson, S. Sathasivam, A. Kafizas, M. Alqahtani, C. Sotelo-Vazquez, J. Buckeridge, J. Wu, S. P. Nair, D. O. Scanlon and I. P. Parkin, *ACS Appl. Mater. Interfaces*, 2020, **12**, 15348–15361.

16 F. H. Aragón, J. A. H. Coaquira, P. Hidalgo, S. L. M. Brito, D. Gouvêa and R. H. R. Castro, *J. Non-Cryst. Solids*, 2010, **356**, 2960–2964.

17 R. D. Shannon, *Acta Crystallogr., Sect. A: Cryst. Phys., Diffr., Theor. Gen. Crystallogr.*, 1976, **32**, 751–767.

18 C. A. Schneider, W. S. Rasband and K. W. Eliceiri, *Nat. Methods*, 2012, **9**, 671–675.

19 F. H. Aragón, P. E. N. de Souza, J. A. H. Coaquira, P. Hidalgo and D. Gouvêa, *Phys. B*, 2012, **407**, 2601–2605.

20 G. Rytwo, R. Zakai and B. Wicklein, *J. Spectrosc.*, 2015, **2015**, 727595.

21 V. Perumal, A. Sabarinathan, R. Robert, K. M. Prabu and R. Uthirakumar, *Mater. Today: Proc.*, 2022, **56**, 3418–3425.

22 R. Scipioni, D. Gazzoli, F. Teocoli, O. Palumbo, A. Paolone, N. Ibris, S. Brutti and M. A. Navarra, *Membranes*, 2014, **4**, 123–142.

23 A. Razeghizadeh, I. Kazemnezhad, L. Zalaghi and V. Rafee, *Iran. J. Chem. Chem. Eng.*, 2018, **37**, 25–32.

24 F. F. H. Aragón, L. Villegas-Lelovsky, J. G. Parizaka, E. G. Zela, R. Bendezu, R. O. Gallegos, D. G. Pacheco-Salazar, S. W. da Silva, R. Cohen, L. C. C. M. Nagamine, J. A. H. Coaquira and P. C. Morais, *Mater. Adv.*, 2023, **4**, 1389–1402.

25 F. H. Aragón, J. A. H. Coaquira, P. Hidalgo, S. W. da Silva, S. L. M. Brito, D. Gouvêa and P. C. Morais, *J. Raman Spectrosc.*, 2011, **42**, 1081–1086.

26 A. Diéguez, A. Romano-Rodríguez, A. Vilà and J. R. Morante, *J. Appl. Phys.*, 2001, **90**, 1550–1557.

27 T. Lan, C. W. Li and B. Fultz, *Phys. Rev. B: Condens. Matter Mater. Phys.*, 2012, **86**, 134302.

28 J. Shen, C. Rao, Z. Fu, X. Feng, J. Liu, X. Fan, H. Peng, X. Xu, C. Tan and X. Wang, *Appl. Surf. Sci.*, 2018, **453**, 204–213.

29 R. H. R. Castro, P. Hidalgo, R. Muccillo and D. Gouvêa, *Appl. Surf. Sci.*, 2003, **214**, 172–177.

30 C. Q. Sun, L. K. Pan, C. M. Li and S. Li, *Phys. Rev. B: Condens. Matter Mater. Phys.*, 2005, **72**, 134301.

31 J. W. Ager, D. K. Veirs and G. M. Rosenblatt, *Phys. Rev. B: Condens. Matter Mater. Phys.*, 1991, **43**, 6491–6499.

32 C. Camus, E. Rudigier, D. Abou-Ras, N. A. Allsop, T. Unold, Y. Tomm, S. Schorr, S. E. Gledhill, T. Köhler, J. Klaer, M. C. Lux-Steiner and C.-H. Fischer, *Appl. Phys. Lett.*, 2008, **92**(10), 101922.

33 I. H. Campbell and P. M. Fauchet, *Solid State Commun.*, 1986, **58**, 739–741.

34 H. T. Girao, P. Hermet, B. Masenelli, J. Haines, P. Mélinon and D. Machon, *Phys. Rev. Lett.*, 2018, **120**, 265702.

35 A. Meulemans, F. Paycha, P. Hannoun and M. Vulpillat, *Antimicrob. Agents Chemother.*, 1989, **33**, 1286–1290.

36 T.-O. Peulen and K. J. Wilkinson, *Environ. Sci. Technol.*, 2011, **45**, 3367–3373.

37 Z. Li, D. Wang, M. Xu, J. Wang, X. Hu, S. Anwar, A. C. Tedesco, P. C. Morais and H. Bi, *J. Mater. Chem. B*, 2020, **8**, 2598–2606.